

Transient energy dissipation at the Fermi velocity in a magnetocaloric metal

Yanna Chen ^{1,2,*},[†] Zhao Zhang^{3,4,*}, Zhe Zhang^{3,4}, Houbo Zhou^{5,6}, Xuexi Yan^{3,4}, Tao Sun⁷, Katherine J. Harmon ⁸, Shigeki Owada^{9,10}, Kensuke Tono^{9,10}, Michihiro Sugahara¹⁰, Osami Sakata ^{11,2}, Michael J. Bedzyk ¹, Chunlin Chen^{3,4}, Zhigao Sheng⁷, Bing Li ^{3,4,‡}, Fengxia Hu^{5,6,§}, Yue Cao ^{8,12,||}, Baogen Shen^{5,6,13} and Zhidong Zhang ^{3,4}

¹Materials Science and Engineering, *Northwestern University, Evanston, Illinois 60201, USA*

²Synchrotron X-ray Group, Research Center for Advanced Measurement and Characterization, *National Institute for Materials Science, 1-1-1 Kouto, Sayo-cho, Sayo-gun, Hyogo 679-5148, Japan*

³Shenyang National Laboratory for Materials Science, *Institute of Metal Research, Chinese Academy of Sciences, 72 Wenhua Road, Shenyang, Liaoning 110016, China*

⁴School of Materials Science and Engineering, *University of Science and Technology of China, 72 Wenhua Road, Shenyang, Liaoning 110016, China*

⁵Beijing National Laboratory for Condensed Matter Physics and State Key Laboratory of Magnetism, *Institute of Physics, Chinese Academy of Sciences, Beijing 100190, China*

⁶School of Physical Sciences, *University of Chinese Academy of Sciences, Beijing 100049, China*

⁷High Magnetic Field Laboratory, HFIPS, *Anhui, Chinese Academy of Sciences, Hefei 230031, China*

⁸Materials Science Division, *Argonne National Laboratory, Lemont, Illinois 60439, USA*

⁹Japan Synchrotron Radiation Research Institute, 1-1-1 Kouto, Sayo-cho, Sayo-gun, Hyogo 679-5148, Japan

¹⁰RIKEN SPring-8 Center, 1-1-1 Kouto, Sayo-cho, Sayo-gun, Hyogo 679-5148, Japan

¹¹Center for Synchrotron Radiation Research, *Japan Synchrotron Radiation Research Institute, 1-1-1 Kouto, Sayo-cho, Sayo-gun, Hyogo 679-5148, Japan*

¹²Pritzker School of Molecular Engineering, *University of Chicago, Chicago, Illinois 60637, USA*

¹³Ningbo Institute of Materials Technology and Engineering, *Chinese Academy of Sciences, Ningbo, Zhejiang 315201, China*



(Received 3 February 2024; accepted 23 September 2024; published 31 October 2024)

Realizing fast energy dissipation in crystalline materials over macroscopic length scales is critical for energy-efficient devices and applications toward a carbon-neutral society but is usually dominated by electron-lattice interactions that cap the energy dissipation at the phonon velocity. Going beyond this velocity has been the focus of many studies, and the physical limit is the Fermi velocity where the energy is predominantly carried away by electrons throughout the materials. However, whether and how the Fermi velocity can be reached over macroscopic distances experimentally remain largely elusive. Here we show ultrafast energy dissipation at the Fermi velocity in the magnetocaloric metal $\text{LaFe}_{10.6}\text{Co}_{1.0}\text{Si}_{1.4}$. Using time-resolved powder x-ray diffraction, we observe negative thermal expansion of the lattice throughout the micron-sized crystals in less than 600 fs with an incident optical fluence higher than 8 J cm^{-2} . The ultrafast timescale is in sharp contrast to the normal energy dissipation and shows the existence of a macroscopic momentum-relaxing electron mean free path immediately after the optical excitation. Our findings open a different regime in energy dissipation and demonstrate the possibility of manipulating macroscopic material properties by strong optical pulses.

DOI: [10.1103/PhysRevB.110.134323](https://doi.org/10.1103/PhysRevB.110.134323)

I. INTRODUCTION

How energy dissipates in solid-state materials is critical for realizing applications and devices with high energy efficiency. On the atomic and nanoscales, energy dissipation is dictated by the electron-electron and electron-lattice interactions and

takes place over ultrafast timescales [1–6]. Over longer distances, the energy dissipation is rate limited by the phonon velocity ($\sim 10^3 \text{ m s}^{-1}$), fundamentally due to the momentum relaxation of electrons from a plethora of scattering events [7–10]. Surpassing the phonon velocity and achieving faster energy dissipation have been the focus of numerous experimental and theoretical studies. Recently, it was demonstrated that energy can travel as fast as several tens of kilometers per second under intense optical excitations, 1 order of magnitude faster than phonons, a phenomenon that was referred to as “transient lattice hydrodynamics” [11]. Achieving energy dissipation at a Fermi velocity of $\sim 10^6 \text{ m s}^{-1}$, $\sim 10^3$ faster than the phonon velocity, is much desired, with huge implications for a wide range of applications from high-speed electronics to civil engineering. Whether such regime can be realized

*These authors contributed equally to this work.

[†]Present address: Canadian Light Source, 44 Innovation Boulevard, Saskatoon, Saskatchewan S7N 2V3, Canada; Contact author: yanna.chen@lightsources.ca

[‡]Contact author: bingli@imr.ac.cn

[§]Contact author: fxhu@iphy.ac.cn

^{||}Contact author: yue.cao@anl.gov

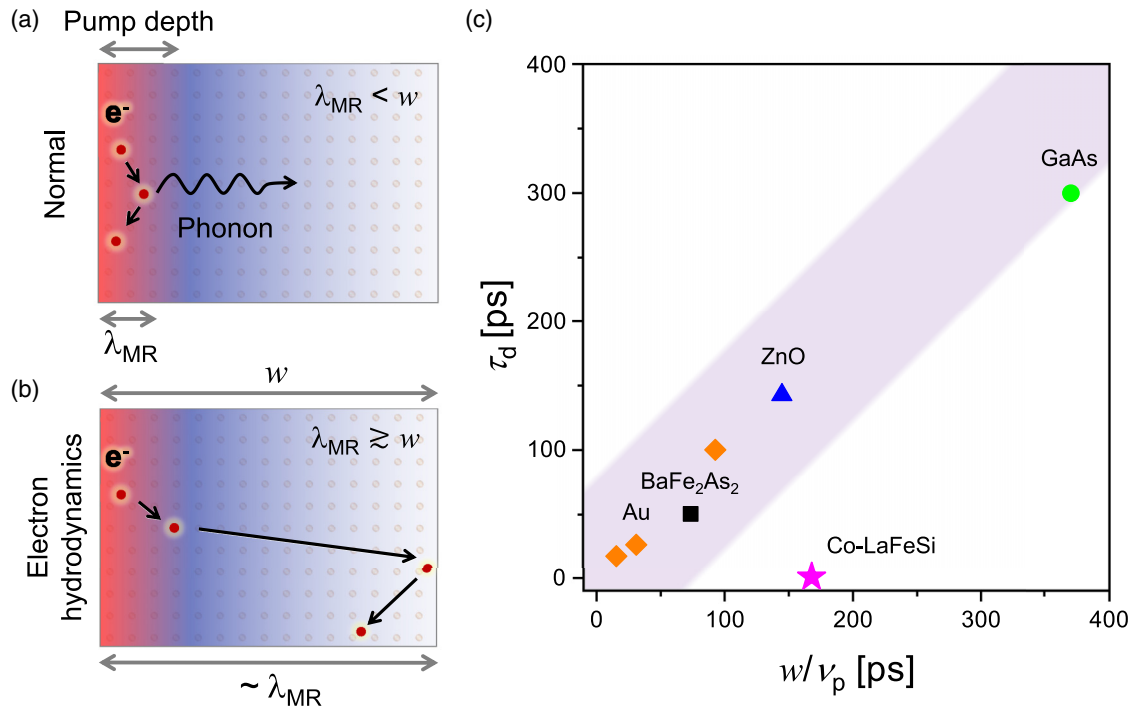


FIG. 1. The energy dissipation velocity across materials where the pump depth is substantially smaller than the probe depth. (a) For normal materials, the electron-phonon scattering leads to the relaxation of the electron momentum. The subsequent energy dissipation is dominated by lattice vibrations at the speed of sound v_p . (b) For energy dissipation at the Fermi velocity, the momentum-relaxing electron mean free path λ_{MR} is comparable to or longer than w , which can be the size of the material or the probe depth, whichever is smaller. Red regime: hot electron; blue regime: cold electron. (c) The characteristic decay timescales τ_d versus w/v_p . The data points are compiled from previous studies in which the probe depth is larger than that of the pump [7–10]. The value of w/v_p from Co-LaFeSi in this work is marked by the purple star.

remains elusive, calling for candidate materials and, equally important, appropriate means of exciting the materials as well as determining the dissipation velocity.

The key physical quantity of interest is the momentum-relaxing electron mean free path λ_{MR} , which includes contributions from events such as electron-phonon scattering and umklapp processes. In normal materials, λ_{MR} is usually substantially smaller than the size of the material. Energy dissipation beyond λ_{MR} is dominated by the lattice, limiting the dissipation velocity. Experimentally determining λ_{MR} and quantifying the energy dissipation is extremely difficult and at equilibrium often relies on careful measurements of the electronic properties with elaborately designed sample geometries [12–16].

With the progress of ultrafast lasers and the advent of x-ray free electron lasers (XFELs), time-resolved studies using nonuniform optical excitations have provided new approaches for assessing the energy dissipation velocity and λ_{MR} . The uniformity of the optical pump or the lack thereof is compared to the area where the probe signal is collected. A nonuniform pump can either be achieved using structured optical excitations including transient grating [17–19] or can be derived from the profile of the pump, e.g., by probing materials at different spatial locations even for a Gaussian laser beam. The latter approach is vital to the discovery of the “transient lattice hydrodynamics” [11].

Optical-pump x-ray-probe experiments provide a natural platform for achieving nonuniform optical excitations, taking advantage of the fact that the optical excitation depth is

usually substantially smaller than the x-ray penetration length. For metals under the excitation of visible light, the optical penetration depth is usually on the order of tens of nanometers. Meanwhile, hard x-ray photons with an energy on the order of 10 keV or higher can probe over tens of microns of solid-state materials. The significant pump-probe-depth mismatch could be utilized to clearly identify the dissipation velocity and λ_{MR} .

To illustrate our idea, we compare the energy dissipation in two regimes with $\lambda_{MR} \ll w$ [Fig. 1(a)] and $\lambda_{MR} \geq w$ [Fig. 1(b)]. Here we use w to denote the x-ray penetration depth or the size of the materials, whichever is smaller. The red and blue regions represent the optically excited and unexcited areas of the material with “hot” and “cold” electrons, respectively. On the order of λ_{MR} , hot electrons transfer energy to the lattice through electron-phonon or umklapp scattering. When $\lambda_{MR} \ll w$, as discussed previously, subsequent energy dissipation is then dominated by phonons [Fig. 1(a)]. The time for the entire material probed by x rays to “warm up” can be estimated to zeroth order as w divided by the sound velocity ($\sim 10^3$ m s $^{-1}$ in solids). In Fig. 1(c), we compile previous studies in which the optical penetration depth is much smaller than the probed depth. Indeed, the characteristic timescales captured by the probe are consistent with the zeroth-order estimate using sound velocities in the respective materials [8,20,21]. In comparison, when $\lambda_{MR} \gg w$, the energy dissipation gets significantly faster [Fig. 1(b)]. Electrons can now travel through the material without interacting with the lattice until they hit the physical boundary of the

crystallite. The duration is fundamentally limited only by the Fermi velocity ($\sim 10^6$ m s $^{-1}$).

In this paper, we determine the speed of energy dissipation in the Co-doped magnetocaloric metal $\text{LaFe}_{13-x}\text{Si}_x$ ($x \sim 1.4$) using time-resolved powder x-ray diffraction (PXRD). Above an incident optical fluence of 8.74 J cm $^{-2}$, we observe lattice thermalization throughout the micron-sized crystals in less than 600 fs. This ultrafast timescale corresponds to the energy dissipation at the Fermi velocity and shows the existence of a macroscopic λ_{MR} at least comparable to the size of the crystallite. Our findings reveal a different regime of energy dissipation and demonstrate the capability of manipulating macroscopic material properties by strong optical pulses.

II. EXPERIMENTAL DETAILS

A. Sample preparation

Polycrystalline Co-LaFeSi was prepared using an arc-melting method followed by long time annealing to reduce the impurity phase of α -Fe, as previously described [22]. The powders were ground, filtered ($\phi = 50$ μm), and examined with scanning electron microscopy (SUPRA 55-VP FEGSEM, Zeiss) and transmission electron microscopy (JEM-2100F, JEOL). The powders were determined to be mostly single crystals with a mean diameter of ~ 1 μm . The phase transition from the ferromagnetic (FM) phase to the paramagnetic (PM) phase was determined using superconducting quantum interference device magnetometry (Quantum Design MPMS XL). Through magnetization at 100 Oe as a function of temperature, the Curie temperature for Co-LaFeSi was determined to be 304 K. Further details of the sample preparation are discussed in the Supplemental Material [23].

B. Time-resolved powder x-ray diffraction

The XFEL experiment was carried out at BL03 of the SPring-8 Angstrom Compact free electron LAsER (SACLA) in Japan [24]. The incident x-ray photon energy was 15 keV (a wavelength of 0.827 \AA) with a pulse repetition rate of 30 Hz. The x-ray beam size was 100 μm in both the horizontal and vertical directions. The x-ray pulse duration was less than 10 fs. The optical pump pulse was generated by a Ti:sapphire laser. An amplifier was added to boost the pulse energy [25]. The pump laser had a wavelength of 800 nm and a repetition rate of 30 Hz. The pulse duration of the pump laser was ~ 30 fs. The pump laser energy used during the measurement was between 143 and 992 μJ per pulse. This optical pulse energy translated to an incident pump fluence between 1.26 and 8.74 J cm $^{-2}$ at the sample position based on the circular laser profile with a diameter of 100 μm and an effective factor (69.2%) imposed by the laser intensity distribution. The experiment was carried out using a high-viscosity sample injector [26,27]. The diffracted powder x-ray diffraction pattern was captured by multiport charge-coupled devices (MPCCDs) [28]. For our measurements, both the Si powder (NIST standard reference material 640c, used to calibrate the MPCCD position and distance relative to the sample) and the Co-LaFeSi powders were filtered ($\phi = 50$ μm) and

then mixed uniformly with a highly viscous DATPE grease acting as a particle carrier [29–31] that is optically transparent to the 800 nm pump laser. The DATPE grease is made of 25 wt % dextrin palmitate (Rheoparl KL2, Chiba Flour Milling Co.) dispersed in dialkyl tetraphenyl ether oil (DATPE, S-3230, MORESCO). The mixed sample was filled into the DAPHNIS injector (inner diameter: 100 μm) and flowed down at a rate of 0.024 mL min $^{-1}$ to provide fresh samples. The injected sample flow was perpendicular to the x ray and the pump laser. The x-ray and the pump laser pulses spatially overlapped in the same region of the grease column. The diffraction images were acquired shot by shot using the MPCCD, and ~ 1000 shots were accumulated at each nominal delay to obtain clear ring patterns prior to the arrival timing jitter correction. The timing jitter between the XFEL and the optical laser pulses was 256 fs [32] and was corrected shot by shot using the timing tool for each PXRD image. After the jitter correction, the time resolution was the convolution of the x-ray and optical pulse durations and was less than 32 fs.

C. Reduction and analysis of the time-resolved PXRD data

The MPCCD detector background was removed from the collected PXRD pattern. We calibrated the sample-to-detector distance (51.8 mm), the position of the direct x-ray beam, and the detector rotation and tilts using the Si standard. With the calibrated parameters, for a given delay, the two-dimensional PXRD patterns from individual XFEL pulses were summed and converted into the one-dimensional PXRD intensity as a function of momentum transfer Q using the PYFAI package [33]. The PXRD background from the grease was further subtracted, resulting in the PXRD intensities displayed in Fig. 2. For a given delay after the optical excitation, each 224 Bragg peak was fitted using two Voigt functions with a linear background. The peak positions of the two Voigt functions were fixed as the 224 Bragg peak in the FM and PM phases. The fitted areas of the Voigt functions were further used to evaluate the FM phase fraction f_{FM} . To obtain the conversion and recovery timescales, we took into account the drift of time zero during the experiment. This drift was determined to be 0.12 ps, consistent with the typical drift at SACLA.

III. RESULTS

$\text{LaFe}_{13-x}\text{Si}_x$ is a canonical giant magnetocaloric metal that has attracted broad attention for its solid-state refrigeration applications [22]. $\text{LaFe}_{13-x}\text{Si}_x$ has a NaZn_{13} type of lattice structure with La atoms caged in Fe/Si clusters [Fig. 2(a), inset]. This lattice structure is known for its poor lattice thermal conduction. Previous studies showed the efficient magnetic-thermal energy conversion in $\text{LaFe}_{13-x}\text{Si}_x$ is attributed to a strong spin-lattice interaction [22,34–36]. Indeed, $\text{LaFe}_{13-x}\text{Si}_x$ features a first-order magnetoelastic phase transition from the FM phase below to the PM phase above the Curie temperature [Fig. 2(a)]. During the transition, the lattice exhibits a discontinuous negative thermal expansion without any lattice symmetry change [37,38]. Specifically, the lattices on both sides of the transition have a fcc structure with

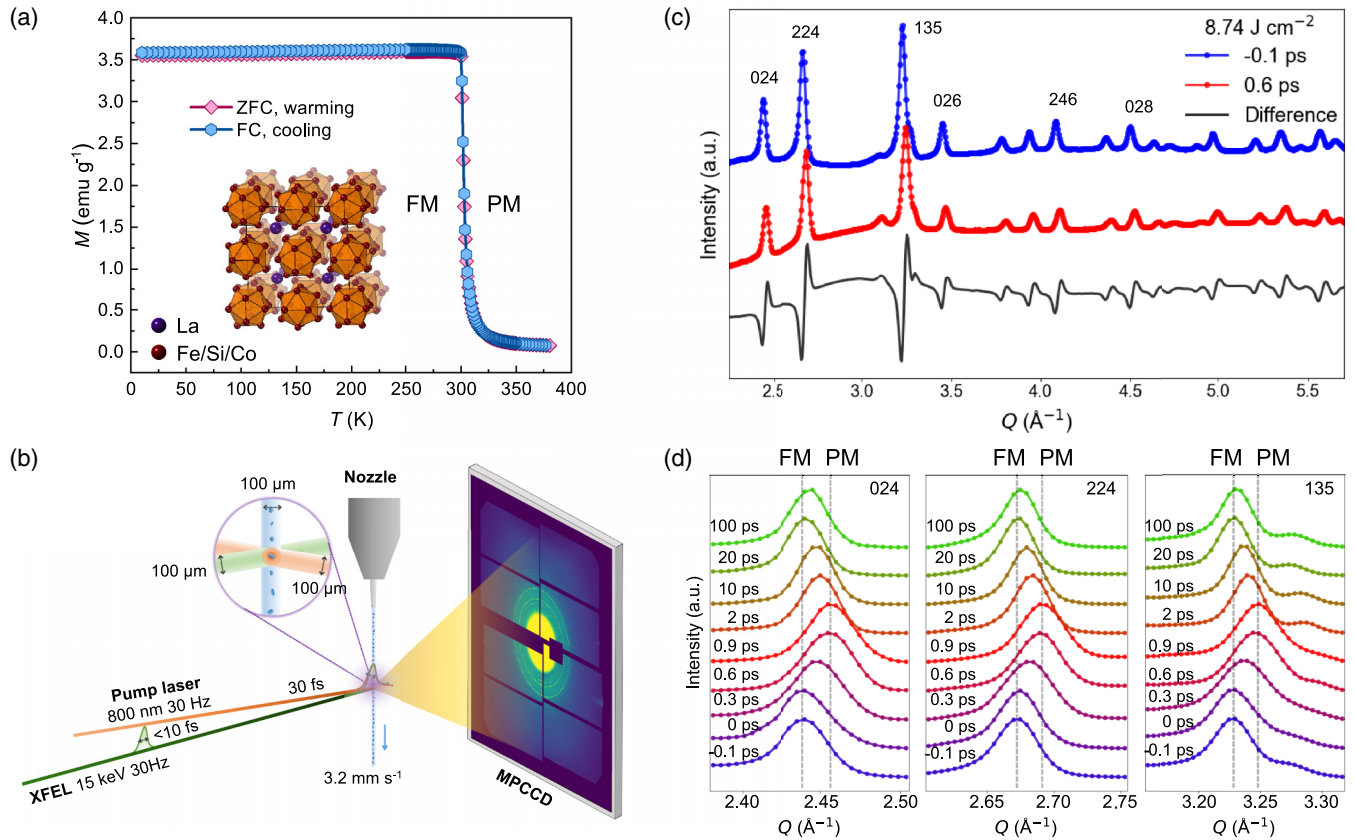


FIG. 2. Ultrafast phase transition in Co-LaFeSi observed using time-resolved powder x-ray diffraction (tr-PXRD). (a) Magnetization measured under zero-field cooling (ZFC; pink diamonds) and field cooling (FC; blue hexagons) as a function of temperature through the ferromagnetic (FM) to paramagnetic (PM) phase transition at thermal equilibrium. (b) Tr-PXRD experimental setup. The powder sample mixed with grease was extruded from a nozzle at a fixed flow rate. Hard x-ray pulses with a photon energy of 15 keV and the 800 nm optical pump laser intersect at the path of the grease column. The ultrafast x-ray and optical laser pulses are synchronized with a repetition rate of 30 Hz. The PXRD patterns were recorded shot to shot using the MPCCD. (c) The PXRD intensity as a function of momentum transfer Q before (at -0.1 ps, blue solid line) and 0.6 ps after (red solid line) the arrival of the optical excitation. The difference between the two PXRD intensities is displayed by the black line, where all the Bragg peaks move toward higher Q after the pump. (d) The temporal evolution of Bragg peaks 024, 224, and 135 under an incident laser fluence of 8.74 J cm^{-2} . The vertical dashed lines mark the peak positions in the FM and PM phases under thermal equilibrium.

the space group $Fm\bar{3}c$ [22]. The Curie temperature can be tuned from ~ 200 up to 350 K by substituting Fe with Co atoms or by adding interstitial hydrogen atoms with minimal magnetic-entropy changes [37,39]. As our time-resolved PXRD (tr-PXRD) setup is limited to room temperature, we selected $\text{LaFe}_{10.6}\text{Co}_{1.0}\text{Si}_{1.4}$ (Co-LaFeSi), with $T_C \sim 304$ K. The contraction of the unit-cell volume of Co-LaFeSi through the magnetic phase transition is determined to be as large as 1% from equilibrium-state powder x-ray diffraction measurements. The details of material synthesis as well as magnetic and structural property characterizations are presented in the Supplemental Material [23].

The tr-PXRD study was carried out at SACLA using the Diverse Application Platform for Hard X-ray Diffraction in SACLA (DAPHINS) system [28] [Fig. 2(b)]. Co-LaFeSi samples were ground into powders and dispersed from the nozzle as a grease column [26,27]. Scanning electron microscopy and transmission electron diffraction studies showed that the majority of the powders are single crystals. A statistical analysis of the particle size distribution revealed that the x-ray diffraction intensity was dominated by crystallites

a few microns in diameter (see the Supplemental Material [23] for details). The 800 nm pump laser and 15 keV probe x-ray photons intersect at the path of the grease column, both with a FWHM of $100 \mu\text{m}$ to match the size of the grease column. The PXRD patterns were acquired in a transmission Debye-Scherrer geometry. Further discussions of the experimental setup and the grease column are presented in the Supplemental Material [23].

We show a typical experimental setup of x-ray diffraction rings from Co-LaFeSi in Fig. 2(b). For a given time delay, the PXRD intensity as a function of momentum transfer Q was derived by summing along the azimuth of the powder ring. In Fig. 2(c) we plot the PXRD intensities before and 0.6 ps after the optical pump with an incident laser fluence of 8.74 J cm^{-2} . The 0.6 ps dataset is displayed because this is when the transient evolution of the PXRD intensity is most pronounced. The difference between the PXRD intensities is also displayed in Fig. 2(c) using the black solid line. After the optical excitation, all the Bragg peaks move toward higher Q in reciprocal space, which corresponds to a contraction of the lattice and signals a laser-induced FM-PM magnetoelastic

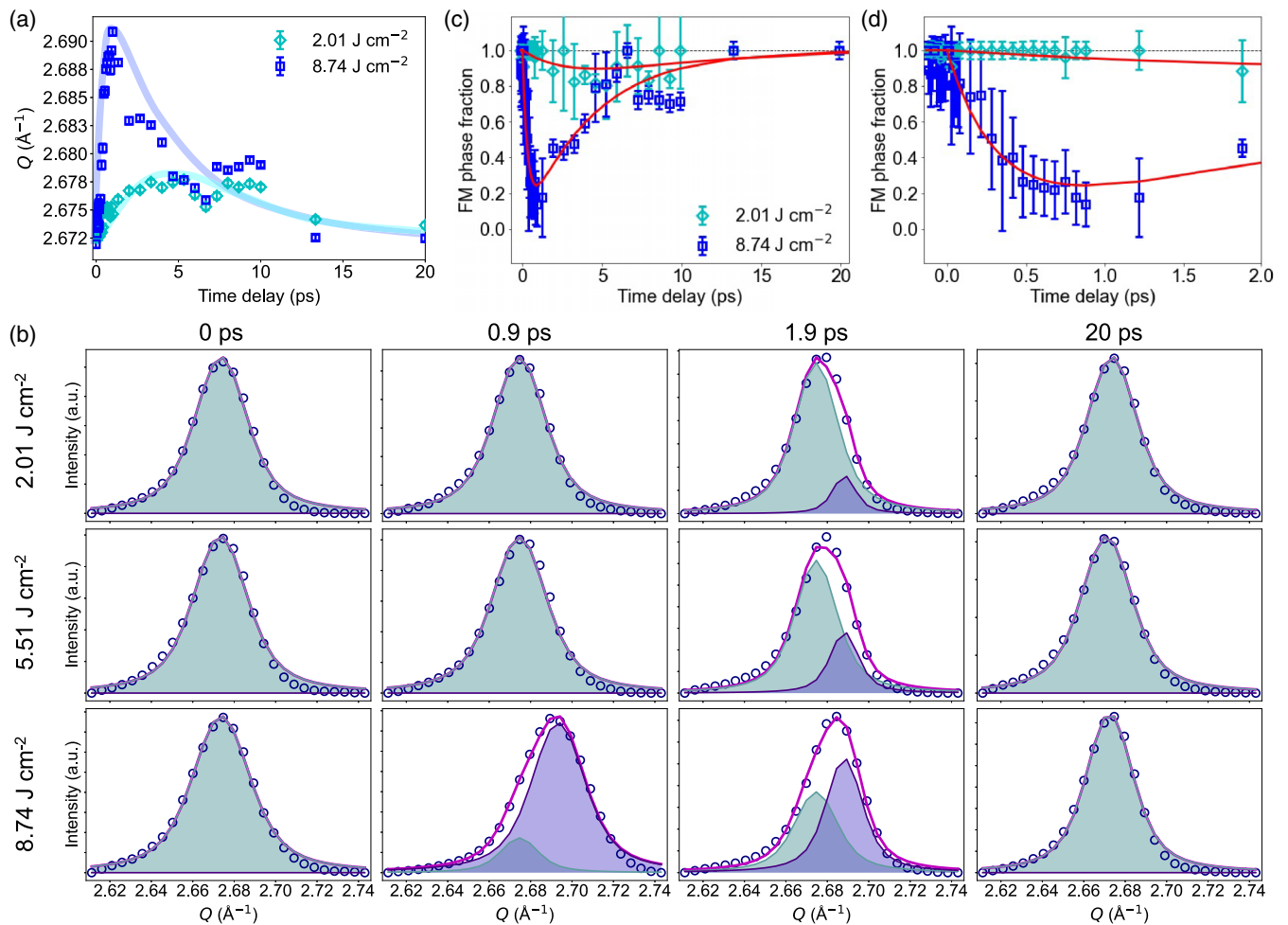


FIG. 3. Ferromagnetic (FM) phase fraction as a function of time delay. (a) The 224 Bragg peak position as a function of time delay at 2.01 and 8.74 J cm⁻². The broad semitransparent lines are guides to the eye. (b) Fitting the 224 Bragg peak with two Voigt functions. The experimental data and the fits are displayed using open circles and solid lines, respectively. The FM and PM phase contributions are marked by the light green and light purple shaded regions. (c) The FM phase fraction as a function of time delay at two laser fluences. (d) A zoomed-in view of the FM phase fraction in (c).

phase transition. Fitting the PXRD in Fig. 2(c) yields lattice constants of 11.517 Å (before) and 11.444 Å (at 0.6 ps), both with the fcc structure. These values are consistent with the lattice constants in the FM and PM phases at thermal equilibrium, within the resolutions of the experimental setups and the refinement methods. Thus, at 0.6 ps and with a pump fluence of 8.74 J cm⁻², Co-LaFeSi converts from the FM phase predominantly to the PM phase. In Fig. 2(d) we show the temporal evolution of three Bragg peaks which are representative of all the measured peaks. To achieve the best time resolution possible (~ 32 fs), the pump-probe delay jitter has been corrected for each x-ray pulse. Details of the data analysis are discussed in the Supplemental Material [23]. All three peaks reach maximum peak shift between 0.6 and 0.9 ps and subsequently move back to lower Q . Note the timescales for the initial conversion (< 0.9 ps) and subsequent recovery (< 20 ps) are substantially faster than phonon-mediated lattice dynamics in materials of similar sizes (on the order of ~ 100 ps) and even faster than dynamics observed in some single-crystalline films less than 10 nm thick (a few picoseconds) [20]. These comparisons indicate that electrons play a

nontrivial role in the energy dissipation and transient dynamics of Co-LaFeSi.

We further study the fluence dependence of this ultrafast phase transition. As the dynamics can be observed at all the Bragg peaks, we focus on the 224 Bragg peak hereafter. In Fig. 3(a), we plot the position of the 224 Bragg peak as a function of delay at the lowest (2.01 J cm⁻²) and highest (8.74 J cm⁻²) fluences used in our study. The FWHMs of the peaks are summarized in the Supplemental Material [23]. At 2.01 J cm⁻², the 224 peak increases from 2.672 Å⁻¹ only up to 2.678 Å⁻¹, smaller than the corresponding Bragg peak position in the PM phase. Because the evolution of the lattice constant is discontinuous across the FM-PM phase transition, from 11.517 to 11.444 Å, at 2.01 J cm⁻² only part of the crystallite is converted into the PM phase. As such, we fit the 224 Bragg peaks as the sum of two Voigt functions centered at $Q = 2.672$ Å⁻¹ and $Q = 2.691$ Å⁻¹. The centers of the two Voigt functions are calculated from the lattice constants in the FM and PM phases. Similar fitting schemes were adopted previously in time-resolved studies of first-order phase transitions with lattice discontinuities [8,19,40]. We show the fitting

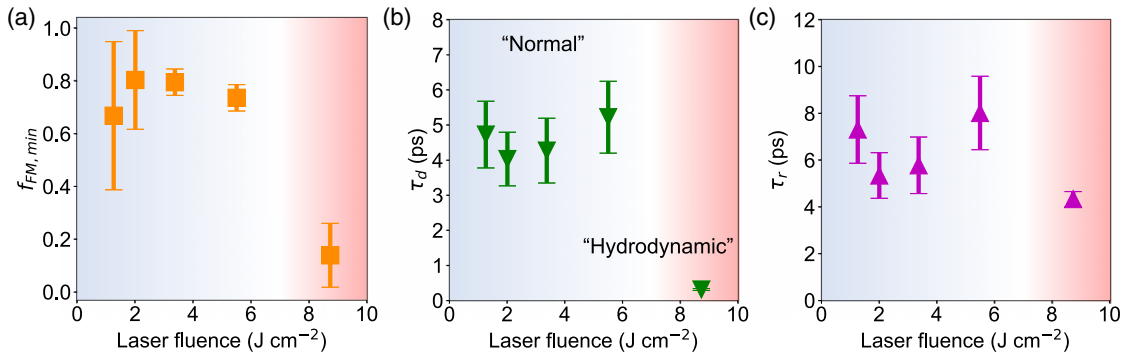


FIG. 4. Characteristic timescales of the decay and recovery processes as a function of incident pump fluence. The minimal fraction of the residual FM phase and the decay τ_d and recovery τ_r timescales are displayed in (a)–(c), respectively.

results for selected pump fluences and delays in Fig. 3(b). Note the Bragg peaks are well defined. Thus, there is no detectable melting of Co-LaFeSi into the liquid phase despite the relatively high laser fluence within the resolution of our measurement. Moreover, that the peak is still well defined at delays as long as 100 ps [Fig. 3(c)] suggests the absence of appreciable laser damage to the sample at least up to 100 ps during the tr-PXRD measurement.

We define the FM phase fraction f_{FM} as the area of the 224 Bragg peak in the FM phase divided by the total intensity of the peak in both phases. The evolution of the f_{FM} as a function of delay at 2.01 and 8.74 J cm⁻² is displayed in Fig. 3(c), with a zoomed-in view of the first 2 ps shown in Fig. 3(d). The initial decay of the FM phase fraction is substantially faster at 8.74 J cm⁻² than at 2.01 J cm⁻², with the minimum FM phase fractions occurring at ~ 0.6 ps and between 4 and 10 ps, respectively. Indeed, it appears a faster decaying component emerges at 8.74 J cm⁻² and “sits” on top of the slower decay at 2.01 J cm⁻² [Fig. 3(c)], reminiscent of the well-known two-temperature model. Notably, the fast and slow decaying components in the conventional two-temperature model in previous studies commonly correspond to the dynamics of the electrons and the lattice, with the effective temperature of the electrons well exceeding that of the lattice immediately after the optical excitation [8,41]. In our case, the resemblance to the two-temperature model is particularly interesting, as PXRD is directly sensitive to only the lattice and not the electron charge or spin. Taken together, these observations indicate the critical role of electrons during energy dissipation at higher pump fluences.

For a more quantitative description of the fluence dependence, we extract three characteristic quantities from the temporal evolution of f_{FM} : (1) the residual FM phase fraction $f_{FM, min}$, which is defined as the minimum FM phase fraction at a given fluence; (2) the decay timescale τ_d ; and (3) the recovery timescale τ_r . τ_d and τ_r are determined using [3,42]

$$f_{FM}(t) = f_{FM}(t < 0)[e^{-t/\tau_d} + (1 - e^{-t/\tau_r})]. \quad (1)$$

Only one timescale each is needed to describe the dynamics and stabilize the fit at lower fluences. For direct comparison, the same set of parameters is used for the highest fluence. Overall, $f_{FM, min}$ reflects the maximum fraction converted to the PM phase, τ_d describes the duration for the optical excitation to dissipate through the material, while τ_r describes

the recovery as the energy subsequently dissipates into the environment.

Figure 4 shows the fluence dependences of these three quantities. Several observations can be made from the fluence dependence. Most prominently, there is a fluence-induced phase transition between 5.51 and 8.74 J cm⁻². Specifically, $f_{FM, min}$ and τ_d remain almost unchanged below 6 J cm⁻² [Figs. 4(a) and 4(b)]. At 8.74 J cm⁻², $f_{FM, min}$ dramatically falls from above 70% to almost zero [Fig. 4(a)], consistent with Fig. 3. Meanwhile, τ_d decreases by more than 1 order of magnitude from ~ 5 to ~ 300 fs [Fig. 4(b)]. In comparison, the recovery time τ_r is almost independent of the incident fluence [Fig. 4(c)], which we assign to the electron-phonon coupling and will detail later. Therefore, it is clear that the transient phase at 8.74 J cm⁻² is qualitatively different from those at lower pump fluences (see the Supplemental Material [23]). However, the only relevant lattice constants from this tr-PXRD study are those of the FM and PM phases, and we are not aware of any other phases, at least at thermal equilibrium. As such, the nature of the transient phase at 8.74 J cm⁻² cannot be distinguished from those below 6 J cm⁻² using known order parameters, i.e., magnetic order or lattice order. Thus, we argue the incident fluence above 8 J cm⁻² excites the material into a new regime without any thermodynamic counterparts.

The defining feature of the new transient regime is that it dissipates energy much faster and more efficiently (with an almost complete conversion to the PM phase) than the “normal” transient phase [Fig. 1(a)]. As the diffraction intensities of the Co-LaFeSi powders are dominated by crystallites a few microns in size, the 15 keV x-ray photons can probe the entire crystal, while the pump laser excites less than the first 100 nm facing the laser. Due to the dramatic pump-probe depth mismatch, the speed of energy dissipation can be estimated using the average size of the particle divided by the time it takes for the side of the particle facing away from the laser to heat up across the phase transition. As an order of magnitude estimate, we use an average particle size of 1 μ m. The duration is chosen to be ~ 600 fs, where f_{FM} reaches the minimum residual FM phase fraction from Fig. 3(c), on the order of τ_d . This gives a speed of energy dissipation of $\sim 10^6$ m s⁻¹. This speed is on the order of the Fermi velocity in a metal but is three orders of magnitude larger than the sound velocity. Strictly speaking, as the electrons must transfer energy to the lattice for the negative

lattice expansion to be observed, 600 fs and τ_d are the upper bounds for the estimate of duration, with 10^6 m s⁻¹ being the lower bound of velocity for energy dissipation mechanisms beyond phonons. Thus, the Fermi velocity is the only relevant speed in materials on this order.

Following Fig. 1, energy dissipation at the Fermi velocity can be realized only when the momentum-relaxing electron mean free path λ_{MR} is greater than or at least comparable to the size of the material w ($\lambda_{\text{MR}} \geq w$). In other words, a statistically significant fraction of electrons needs to travel from the optically excited area to the “cold” regions through the micron-sized material without scattering with the lattice to *simultaneously* account for the nearly complete phase conversion and the ultrafast τ_d . We use the word “statistically” to acknowledge that even within λ_{MR} , electron-phonon or umklapp scattering processes can still take place. In fact, assuming these scatterings are Markovian, λ_{MR} can be longer than the size of the crystallite as long as, e.g., the momentum-relaxing scattering events account for less than $1 - 1/e = 63\%$ of all scattering events. Given the chemical disorder from Si and Co substitutions of the Fe site in the unit cell, some electrons will unavoidably scatter with local lattice defects and imperfections. These scattering events are momentum relaxing in nature and lead to the energy transfer to the lattice, giving rise to a local (e.g., tens of nanometers or less) FM-PM phase transition. These local phase transitions allow the entire crystallite to transform within 600 fs, without having to wait for heat transfer from the boundary of the crystallite.

To highlight the ultrafast timescale in this work, we compare the structural evolution in Co-LaFeSi to previous pump-probe studies in other ferromagnetic materials. Performed in the pump-probe volume-matched regime and often for thin-film materials, past studies reported the electrons lose ferromagnetism much faster than 1 ps and are usually time resolution limited [43–47]. However, the thermalization and subsequent recovery of the lattice take place substantially more slowly than those of the electrons and can extend well over tens of picoseconds. The ultrafast lattice response in Co-LaFeSi deep in the pump-probe mismatched regime is therefore highly unusual and reflects the strong electron-lattice coupling and, ultimately, the superior magnetocaloric property in the material.

We further compare the energy dissipation in this work to that reported in noble metals. Previously, Brorson *et al.* [48] discovered energy dissipation at the Fermi velocity in gold films with thicknesses of a few hundred nanometers at a relatively modest pump fluence on the order of a few millijoules per square centimeter. However, gold is known for its superior electrical conductivity. The low pump fluences did not lead to any phase transition in the gold. With much higher pump fluences greater than 100 mJ cm⁻² [8], which were enough to induce the phase transition, the lattice response slowed down to ~ 50 ps, and the grain boundaries in the film led to momentum-relaxing electron scattering. This comparison adds to the significance of this work, with Fermi velocity energy dissipation occurring despite even higher (> 8 J cm⁻²) pump fluences.

Now that we have clarified the nature of the transient phase and the role of electrons, we examine the role of the lattice and electron-lattice interactions. From Fig. 4(c), the recovery

timescale τ_r is around 5 ps and essentially independent of pump fluence. Also, in the normal transient phase, τ_d is almost identical to τ_r . Thus, the ~ 5 ps timescale most likely arises from the same origin. We can rule out this timescale as being solely from phonons. Following the speed of sound argument, a phonon-dominated timescale should be at least on the order of hundreds of picoseconds over micrometer length scales [8,20]. Also, to zeroth order, PXR is not sensitive to the magnetic degree of freedom. Therefore, electron-phonon coupling is the most likely interaction corresponding to the ~ 5 ps timescale. Our assignment is consistent with the lack of fluence dependence, as the timescale of electron-phonon interaction is fundamentally related to the strength of this interaction [3,49].

Interestingly, no phonon-dominated recovery timescales were observed in our experiment, in contrast to what was reported in a wide range of other materials [3,20,21]. While such a slow recovery process may still exist, within our experimental resolution, the PXR peak position and the intensity mostly recover by 20 ps [Figs. 2(d), 3(a), 3(c) and 3(d)]. Phonon-dominated energy dissipation at best plays a very minor role in Co-LaFeSi single crystallites. This may be due to the complex crystal structure of the LaFe_{13-x}Si_x family. As discussed previously, the La atoms are trapped in Fe/Si/Co cages. This type of cage structure is known to give rise to reduced lattice thermal conductivity [50,51]. Since the lattice does not conduct energy efficiently, electron-phonon coupling overtakes phonons as the major channel for energy dissipation. For the LaFe_{13-x}Si_x family, the strong coupling and coherent energy exchange between the electrons and the lattice not only explain the absence of slow recovery but may also correlate with the small thermal hysteresis of the material. For magnetocaloric materials, the first-order phase transitions are usually desirable due to the large magnetic entropy changes [22], while most first-order phase transitions feature sizable intrinsic thermal hysteresis. It is fundamentally challenging to simultaneously optimize the overall magnetocaloric properties to achieve larger magnetic entropy changes and smaller thermal hysteresis. Here the combination of negligible thermal hysteresis shown in Fig. 2(a) and the magnetic entropy changes larger than 20 J kg⁻¹ K⁻¹ makes the LaFe_{13-x}Si_x family unique. In this sense, it is tempting to explore systems with first-order phase transitions and strong electron-lattice coupling as future magnetocaloric materials. Moreover, it would be attractive to discover more examples of ultrafast energy dissipations in such materials.

IV. DISCUSSION

Our key observation is a regime of energy dissipation at the Fermi velocity, which amounts to a momentum-relaxing electron mean free path $\lambda_{\text{MR}} \geq w$. We propose this regime is intimately related to the much anticipated “transient electron hydrodynamics.” At thermal equilibrium, electron hydrodynamics features “liquidlike” electron transport [15,52–55] that simultaneously satisfies $\lambda_{\text{MR}} > w > \lambda_{\text{MC}}$, where λ_{MC} is the momentum-conserving electron mean free path. Until recently, electron hydrodynamics has been discovered only in a handful of materials at thermal equilibrium under cryogenic temperatures [12–16,56–59]. This is because

both λ_{MR} and λ_{MC} decrease rapidly with increasing temperature. At room temperatures, most metals have λ_{MC} and λ_{MR} smaller than the sample size and behave as normal metals. In our case, away from equilibrium, optical excitation usually leads to an ultrafast increase in the electron temperature, making our observation of $\lambda_{MR} \geq w$ in Co-LaFeSi extremely striking. Since both our work and previous studies on electron hydrodynamics concern $\lambda_{MR} \geq w$ and since the energy dissipation is much faster than the transient lattice hydrodynamics [11], it is plausible to name the energy dissipation at the Fermi velocity in this work “transient electron hydrodynamics.”

Admittedly, our measurements were not sensitive to λ_{MC} , and determining λ_{MC} in a transient state is highly nontrivial. However, λ_{MC} is most likely much smaller than the size of the crystallite in the transient state. At room temperature and over a wide temperature range, the LaFeSi family (including Co-LaFeSi) is a bad metal, with a resistivity on the order of $10^{-4} \Omega \text{ cm}$ [60,61]. This number is 3 orders higher than that of typical elemental metals. e.g., gold, silver, and copper. At room temperature, the electron mean free paths for these noble metals are all in the vicinity of $\sim 50 \text{ nm}$ [62]. Therefore, the total electron mean free path for the LaFeSi family is expected to be less than 10 nm, which includes contributions from both λ_{MC} and λ_{MR} . For the LaFeSi family, λ_{MC} is dominated by the strong magnetic interactions in the material [63] and is expected to be on the same order as the total electron mean free path. Moreover, upon photoexcitation, λ_{MC} is proportional to T_e^{-2} , where T_e is the effective electron temperature. Taken together, it is plausible that $\lambda_{MC} \ll w$ above 8 J cm^{-2} and most likely for the entire range of optical fluence. Our observation is in marked contrast to both the normal and ballistic electron transport regimes and suggests electrons exhibit hydrodynamic behavior under the strong optical excitation. Thus, we refer to the optically induced phase above and below $\sim 8 \text{ J cm}^{-2}$ as “hydrodynamic” and “normal,” respectively [Fig. 4(b)].

To sum up, we discovered an ultrafast energy dissipation at the Fermi velocity in micron-sized Co-LaFeSi crystals arising directly from a macroscopic λ_{MR} over distances comparable

to or larger than the size of the material, which indicates transient electron hydrodynamic behavior. While it is unclear why similar transient phenomena were not observed in “purer” metals with higher electron mobility, e.g., platinum or gold, our observations provide an avenue toward realizing electron hydrodynamics away from thermal equilibrium and will inspire theoretical and experimental investigations into the general notions and microscopic descriptions of transient electron hydrodynamics.

ACKNOWLEDGMENTS

The work conducted at the Institute of Metal Research was supported by the Ministry of Science and Technology of China (Grants No. 2021YFB3501201 and No. 2022YFE0109900), the Key Research Program of Frontier Sciences of the Chinese Academy of Sciences (Grant No. ZDBS-LY-JSC002), and the International Partner Program of the Chinese Academy of Sciences (Grant No. 174321KYSB20200008). The work conducted at the Institute of Physics was supported by the Ministry of Science and Technology of China (Grant No. 2021YFB3501202) and the National Natural Science Foundation of China (Grants No. U1832219 and No. 52088101). Y. Chen and M.J.B. were supported by the Northwestern University (NU) Institute of Catalysis in Energy Processes, which is funded by the U.S. Department of Energy, Office of Science, Office of Basic Energy Sciences, under Award No. DE-FG02-03ER15457. O.S. was supported by Grants-in-Aid for Scientific Research (C), Grant No. 18K04868. The analysis and interpretation of the experiment at SACLA were supported in part by the U.S. Department of Energy, Office of Science, Basic Energy Sciences, Materials Science and Engineering Division. K.J.H. was supported by Laboratory Directed Research and Development (LDRD) funding from Argonne National Laboratory, provided by the Director, Office of Science, of the U.S. Department of Energy under Contract No. DE-AC02-06CH11357. We acknowledge beam time awarded by SACLA (Proposals No. 2019A8092 and No. 2019B8077). Y. Cao also thanks I. K. Robinson for helpful discussions.

-
- [1] A. de la Torre, D. M. Kennes, M. Claassen, S. Gerber, J. W. McIver, and M. A. Sentef, *Colloquium: Nonthermal pathways to ultrafast control in quantum materials*, *Rev. Mod. Phys.* **93**, 041002 (2021).
 - [2] R. Mankowsky *et al.*, Nonlinear lattice dynamics as a basis for enhanced superconductivity in $\text{YBa}_2\text{Cu}_3\text{O}_{6.5}$, *Nature (London)* **516**, 71 (2014).
 - [3] M. Dean *et al.*, Ultrafast energy- and momentum-resolved dynamics of magnetic correlations in the photo-doped Mott insulator Sr_2IrO_4 , *Nat. Mater.* **15**, 601 (2016).
 - [4] S. Gerber *et al.*, Femtosecond electron-phonon lock-in by photoemission and x-ray free-electron laser, *Science* **357**, 71 (2017).
 - [5] P. Tengdin *et al.*, Critical behavior within 20 fs drives the out-of-equilibrium laser-induced magnetic phase transition in nickel, *Sci. Adv.* **4**, eaap9744 (2018).
 - [6] A. Sood *et al.*, Universal phase dynamics in VO_2 switches revealed by ultrafast operando diffraction, *Science* **373**, 352 (2021).
 - [7] T. Suzuki *et al.*, Ultrafast optical stress on BaFe_2As_2 , *Phys. Rev. Res.* **3**, 033222 (2021).
 - [8] T. A. Assefa *et al.*, Ultrafast x-ray diffraction study of melt-front dynamics in polycrystalline thin films, *Sci. Adv.* **6**, eaax2445 (2020).
 - [9] X. Wu, J. Lee, V. Varshney, J. L. Wohlwend, A. K. Roy, and T. Luo, Thermal conductivity of wurtzite zinc-oxide from first-principles lattice dynamics—a comparative study with gallium nitride, *Sci. Rep.* **6**, 22504 (2016).
 - [10] C. Rose-Petruck, R. Jimenez, T. Guo, A. Cavalleri, C. W. Siders, F. Rksi, J. A. Squier, B. C. Walker, K. R. Wilson, and C. P. Barty, Picosecond–milliångström lattice dynamics measured by ultrafast x-ray diffraction, *Nature (London)* **398**, 310 (1999).

- [11] J. Jeong, X. Li, S. Lee, L. Shi, and Y. Wang, Transient hydrodynamic lattice cooling by picosecond laser irradiation of graphite, *Phys. Rev. Lett.* **127**, 085901 (2021).
- [12] P. J. Moll, P. Kushwaha, N. Nandi, B. Schmidt, and A. P. Mackenzie, Evidence for hydrodynamic electron flow in PdCoO₂, *Science* **351**, 1061 (2016).
- [13] A. Lucas and K. C. Fong, Hydrodynamics of electrons in graphene, *J. Phys.: Condens. Matter* **30**, 053001 (2018).
- [14] J. A. Sulpizio *et al.*, Visualizing Poiseuille flow of hydrodynamic electrons, *Nature (London)* **576**, 75 (2019).
- [15] G. Varnavides, A. S. Jermyn, P. Anikeeva, C. Felser, and P. Narang, Electron hydrodynamics in anisotropic materials, *Nat. Commun.* **11**, 4710 (2020).
- [16] M. J. Ku *et al.*, Imaging viscous flow of the Dirac fluid in graphene, *Nature (London)* **583**, 537 (2020).
- [17] F. Hofmann, M. P. Short, and C. A. Dennett, Transient grating spectroscopy: An ultrarapid, nondestructive materials evaluation technique, *MRS Bull.* **44**, 392 (2019).
- [18] F. Bencivenga *et al.*, Nanoscale transient gratings excited and probed by extreme ultraviolet femtosecond pulses, *Sci. Adv.* **5**, eaaw5805 (2019).
- [19] T. D. Frazer *et al.*, Optical transient grating pumped x-ray diffraction microscopy for studying mesoscale structural dynamics, *Sci. Rep.* **11**, 19322 (2021).
- [20] M. Mo *et al.*, Heterogeneous to homogeneous melting transition visualized with ultrafast electron diffraction, *Science* **360**, 1451 (2018).
- [21] M. Mo, S. Murphy, Z. Chen, P. Fossati, R. Li, Y. Wang, X. Wang, and S. Glenzer, Visualization of ultrafast melting initiated from radiation-driven defects in solids, *Sci. Adv.* **5**, eaaw0392 (2019).
- [22] B. Shen, J. Sun, F. Hu, H. Zhang, and Z. Cheng, Recent progress in exploring magnetocaloric materials, *Adv. Mater.* **21**, 4545 (2009).
- [23] See Supplemental Material at <http://link.aps.org/supplemental/10.1103/PhysRevB.110.134323> for further details about the material characterization, data analysis, and optical studies.
- [24] T. Ishikawa *et al.*, A compact x-ray free-electron laser emitting in the sub-ångström region, *Nat. Photon.* **6**, 540 (2012).
- [25] K. Tono *et al.*, Beamline, experimental stations and photon beam diagnostics for the hard x-ray free electron laser of SACLA, *New J. Phys.* **15**, 083035 (2013).
- [26] Y. Shimazu *et al.*, High-viscosity sample-injection device for serial femtosecond crystallography at atmospheric pressure, *J. Appl. Crystallogr.* **52**, 1280 (2019).
- [27] M. Sugahara *et al.*, Grease matrix as a versatile carrier of proteins for serial crystallography, *Nat. Methods* **12**, 61 (2015).
- [28] K. Tono *et al.*, Diverse application platform for hard x-ray diffraction in SACLA (DAPHNIS): Application to serial protein crystallography using an x-ray free-electron laser, *J. Synchrotron Radiat.* **22**, 532 (2015).
- [29] J.-P. Colletier *et al.*, Serial femtosecond crystallography and ultrafast absorption spectroscopy of the photoswitchable fluorescent protein IrisFP, *J. Phys. Chem. Lett.* **7**, 882 (2016).
- [30] M. Suga *et al.*, Light-induced structural changes and the site of O = O bond formation in PSII caught by XFEL, *Nature (London)* **543**, 131 (2017).
- [31] M. Sugahara, K. Motomura, M. Suzuki, T. Masuda, Y. Joti, K. Numata, K. Tono, M. Yabashi, and T. Ishikawa, Viscosity-adjustable grease matrices for serial nanocrystallography, *Sci. Rep.* **10**, 1371 (2020).
- [32] T. Katayama *et al.*, A beam branching method for timing and spectral characterization of hard x-ray free-electron lasers, *Struct. Dyn.* **3**, 034301 (2016).
- [33] G. Ashiotis, A. Deschildre, Z. Nawaz, J. P. Wright, D. Karkoulis, F. E. Picca, and J. Kieffer, The fast azimuthal integration Python library: pyFAI, *J. Appl. Crystallogr.* **48**, 510 (2015).
- [34] F.-X. Hu, B.-G. Shen, J.-R. Sun, Z.-H. Cheng, G.-H. Rao, and X.-X. Zhang, Influence of negative lattice expansion and metamagnetic transition on magnetic entropy change in the compound LaFe_{11.4}Si_{1.6}, *Appl. Phys. Lett.* **78**, 3675 (2001).
- [35] J. Liu, T. Gottschall, K. P. Skokov, J. D. Moore, and O. Gutfleisch, Giant magnetocaloric effect driven by structural transitions, *Nat. Mater.* **11**, 620 (2012).
- [36] M. E. Gruner *et al.*, Element-resolved thermodynamics of magnetocaloric LaFe_{13-x}Si_x, *Phys. Rev. Lett.* **114**, 057202 (2015).
- [37] F. Hu, J. Gao, X. Qian, M. Ilyn, A. Tishin, J. Sun, and B. Shen, Magnetocaloric effect in itinerant electron metamagnetic systems La(Fe_{1-x}Co_x)_{11.9}Si_{1.1}, *J. Appl. Phys.* **97**, 10M303 (2005).
- [38] T. Faske, I. A. Radulov, M. Hölzel, O. Gutfleisch, and W. Donner, Direct observation of paramagnetic spin fluctuations in LaFe_{13-x}Si_x, *J. Phys.: Condens. Matter* **32**, 115802 (2020).
- [39] A. Fujita, S. Fujieda, Y. Hasegawa, and K. Fukamichi, Itinerant-electron metamagnetic transition and large magnetocaloric effects in La(Fe_xSi_{1-x})₁₃ compounds and their hydrides, *Phys. Rev. B* **67**, 104416 (2003).
- [40] S. O. Mariager *et al.*, Structural and magnetic dynamics of a laser induced phase transition in FeRh, *Phys. Rev. Lett.* **108**, 087201 (2012).
- [41] I. Robinson, J. Clark, and R. Harder, Materials science in the time domain using Bragg coherent diffraction imaging, *J. Opt.* **18**, 054007 (2016).
- [42] A. Cavalleri, C. Tóth, C. W. Siders, J. A. Squier, F. Ráksi, P. Forget, and J. C. Kieffer, Femtosecond structural dynamics in VO₂ during an ultrafast solid-solid phase transition, *Phys. Rev. Lett.* **87**, 237401 (2001).
- [43] M. Djordjevic, M. Lüttich, P. Moschkau, P. Guderian, T. Kampfrath, R. Ulbrich, M. Münzenberg, W. Felsch, and J. Moodera, Comprehensive view on ultrafast dynamics of ferromagnetic films, *Phys. Status Solidi C* **3**, 1347 (2006).
- [44] M. Krauß, T. Roth, S. Alebrand, D. Steil, M. Cinchetti, M. Aeschlimann, and H. C. Schneider, Ultrafast demagnetization of ferromagnetic transition metals: The role of the Coulomb interaction, *Phys. Rev. B* **80**, 180407(R) (2009).
- [45] S. Eich *et al.*, Band structure evolution during the ultrafast ferromagnetic-paramagnetic phase transition in cobalt, *Sci. Adv.* **3**, e1602094 (2017).
- [46] D. Zahn *et al.*, Lattice dynamics and ultrafast energy flow between electrons, spins, and phonons in a 3D ferromagnet, *Phys. Rev. Res.* **3**, 023032 (2021).
- [47] R. S. Malik *et al.*, Ultrafast magnetization dynamics in the half-metallic Heusler alloy Co₂FeAl, *Phys. Rev. B* **104**, L100408 (2021).
- [48] S. D. Brorson, J. G. Fujimoto, and E. P. Ippen, Femtosecond electronic heat-transport dynamics in thin gold films, *Phys. Rev. Lett.* **59**, 1962 (1987).
- [49] P. B. Allen, Theory of thermal relaxation of electrons in metals, *Phys. Rev. Lett.* **59**, 1460 (1987).

- [50] G. Nolas, D. Morelli, and T. M. Tritt, Skutterudites: A phonon-glass-electron crystal approach to advanced thermoelectric energy conversion applications, *Annu. Rev. Mater. Sci.* **29**, 89 (1999).
- [51] J. L. Feldman, D. J. Singh, I. I. Mazin, D. Mandrus, and B. C. Sales, Lattice dynamics and reduced thermal conductivity of filled skutterudites, *Phys. Rev. B* **61**, R9209 (2000).
- [52] R. N. Gurzhi, Minimum of resistance in impurity-free conductors, *J. Exp. Theor. Phys.* **44**, 771 (1963).
- [53] L. Levitov and G. Falkovich, Electron viscosity, current vortices and negative nonlocal resistance in graphene, *Nat. Phys.* **12**, 672 (2016).
- [54] D. Di Sante, J. Erdmenger, M. Greiter, I. Matthaiakakis, R. Meyer, D. R. Fernández, R. Thomale, E. van Loon, and T. Wehling, Turbulent hydrodynamics in strongly correlated kagome metals, *Nat. Commun.* **11**, 3997 (2020).
- [55] E. H. Hasdeo, J. Ekström, E. G. Idrisov, and T. L. Schmidt, Electron hydrodynamics of two-dimensional anomalous Hall materials, *Phys. Rev. B* **103**, 125106 (2021).
- [56] J. Crossno *et al.*, Observation of the Dirac fluid and the breakdown of the Wiedemann-Franz law in graphene, *Science* **351**, 1058 (2016).
- [57] R. K. Kumar *et al.*, Superballistic flow of viscous electron fluid through graphene constrictions, *Nat. Phys.* **13**, 1182 (2017).
- [58] J. Gooth, F. Menges, N. Kumar, V. Süß, C. Shekhar, Y. Sun, U. Drechsler, R. Zierold, C. Felser, and B. Gotsmann, Thermal and electrical signatures of a hydrodynamic electron fluid in tungsten diphosphide, *Nat. Commun.* **9**, 4093 (2018).
- [59] U. Vool *et al.*, Imaging phonon-mediated hydrodynamic flow in WTe₂, *Nat. Phys.* **17**, 1216 (2021).
- [60] H. Wang, R. Huang, and L. Li, Low-temperature coefficient of resistivity in LaFe_{13-x}Si_x compounds, *Cryogenics* **108**, 103088 (2020).
- [61] F.-X. Hu, X.-L. Qian, G.-J. Wang, J.-R. Sun, B.-G. Shen, Z.-H. Cheng, and J. Gao, Magnetoresistances and magnetic entropy changes associated with negative lattice expansions in NaZn₁₃-type compounds LaFeCoSi, *Chin. Phys.* **14**, 2329 (2005).
- [62] D. Gall, Electron mean free path in elemental metals, *J. Appl. Phys.* **119**, 085101 (2016).
- [63] Z. Zhang *et al.*, Intense ferromagnetic fluctuations preceding magnetoelastic first-order transitions in giant magnetocaloric LaFe_{13-x}Si_x, *Phys. Rev. Mater.* **5**, L071401 (2021).